

# Diffusion Models for Contrast Harmonization of Magnetic Resonance Images

Alicia Durrer<sup>1</sup>

ALICIA.DURRER@UNIBAS.CH

Julia Wolleb<sup>1</sup>

JULIA.WOLLEB@UNIBAS.CH

Florentin Bieder<sup>1</sup>

FLORENTIN.BIEDER@UNIBAS.CH

Tim Sinnecker<sup>1,2</sup>

TIM.SINNECKER@USB.CH

Matthias Weigel<sup>1,2</sup>

MATTHIAS.WEIGEL@UNIBAS.CH

Robin Sandkühler<sup>1</sup>

ROBIN.SANDKUEHLER@UNIBAS.CH

Cristina Granziera<sup>1,2</sup>

CRISTINA.GRANZIERA@USB.CH

Özgür Yaldizli<sup>1,2</sup>

OEZGUER.YALDIZLI@USB.CH

Philippe C. Cattin<sup>1</sup>

PHILIPPE.CATTIN@UNIBAS.CH

<sup>1</sup> *Department of Biomedical Engineering, University of Basel, Allschwil, Switzerland*

<sup>2</sup> *University Hospital Basel, Switzerland*

## Abstract

Magnetic resonance (MR) images from multiple sources often show differences in image contrast related to acquisition settings or the used scanner type. For long-term studies, longitudinal comparability is essential but can be impaired by these contrast differences, leading to biased results when using automated evaluation tools. This study presents a diffusion model-based approach for contrast harmonization. We use a data set consisting of scans of 18 Multiple Sclerosis patients and 22 healthy controls. Each subject was scanned in two MR scanners of different magnetic field strengths (1.5 T and 3 T), resulting in a paired data set that shows scanner-inherent differences. We map images from the source contrast to the target contrast for both directions, from 3 T to 1.5 T and from 1.5 T to 3 T. As we only want to change the contrast, not the anatomical information, our method uses the original image to guide the image-to-image translation process by adding structural information. The aim is that the mapped scans display increased comparability with scans of the target contrast for downstream tasks. We evaluate this method for the task of segmentation of cerebrospinal fluid, grey matter and white matter. Our method achieves good and consistent results for both directions of the mapping.

**Keywords:** Diffusion models, contrast harmonization, image-to-image translation

## 1. Introduction

In medical studies using magnetic resonance (MR) images, data acquisition from multiple centers and different scanners is a common scenario, especially regarding comprehensive or long-term studies (Krüger et al., 2020). However, challenges arise when we compare data acquired with different MR scanners since the obtained MR images often display differences related to the acquisition settings and scanner variability (Dadar et al., 2020). For instance, as the magnetic field strength alters the level of contrast between different tissue types (Maubon et al., 1999; Ba-Ssalamah et al., 2003), the location of borders between different tissues can vary in images acquired with MR scanners of different field strength (Keihaninejad et al., 2010). Therefore, direct comparison of scans from different scanners

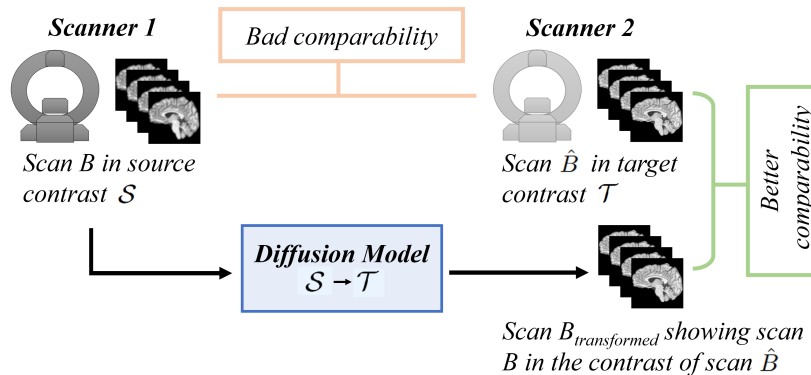


Figure 1: Overview of our contrast harmonization method. We train a diffusion model using paired data from source contrast  $\mathcal{S}$  and target contrast  $\mathcal{T}$ . We translate scan  $B \in \mathcal{S}$  to scan  $B_{transformed}$  that appears in contrast  $\mathcal{T}$ , allowing better comparability with  $\hat{B} \in \mathcal{T}$  in subsequent tasks, such as segmentation.

with automated tools such as SIENA (Smith et al., 2002, 2004) is highly difficult. Consequently, a scanner change in the middle of a long-term study affects the automatic evaluation and longitudinal comparability of scans (Sinnecker et al., 2022). Longitudinal studies are important to monitor progressive diseases such as Multiple Sclerosis (MS), a demyelinating central nervous system disease (Mahad et al., 2015). It is essential that subsequent scans allow reliable interpretation of the disease progression without a bias related to a scanner change between the image acquisitions. In this work, we focus on a scanner change from 1.5 T to 3 T magnetic field strength that took place within a longitudinal MS study (Disanto et al., 2016). The goal of this work is to restore the comparability of the images by mapping all images to the same target contrast. A data set was acquired by (Sinnecker et al., 2022), for which healthy subjects as well as MS patients were scanned in the 1.5 T and the 3 T scanner within approximately 3.5 months. Due to the short time span between the acquisitions, we assume that the differences in the images of the same participant are only related to the different scanner types. We therefore have paired 1.5 T and 3 T data for each participant.

**Contribution** By adapting a Denoising Diffusion Probabilistic Model (DDPM) (Ho et al., 2020; Wolleb et al., 2022b) for contrast harmonization, we translate images from a source contrast  $\mathcal{S}$  to a target contrast  $\mathcal{T}$ . Considering a pair  $B \in \mathcal{S}$ ,  $\hat{B} \in \mathcal{T}$ , we map scan  $B$  slice-by-slice to scan  $B_{transformed}$ , appearing in the contrast of  $\mathcal{T}$ , as shown in Figure 1. We generate consistent three-dimensional (3D) volumes by stacking two-dimensional (2D) slices, allowing us to save memory during image-to-image translation. Compared to the original  $B$ ,  $B_{transformed}$  presents better comparability with  $\hat{B}$  from  $\mathcal{T}$ , with respect to downstream tasks such as segmentation of grey matter (GM), white matter (WM) and cerebrospinal fluid (CSF) using FAST (Zhang et al., 2001). We achieve good results for both directions of the mapping, i.e., from 3 T to 1.5 T and from 1.5 T to 3 T.

**Related Work** Tracking brain volume changes over different scanners is prone to an error related to the scanner change (Lee et al., 2019). (Sinnecker et al., 2022) showed that given a paired data set, a corrective term for the volume computation can be calculated. To achieve a higher level of generalizability, images should be mapped to the target contrast. DeepHarmony (Dewey et al., 2019), builds on the U-Net architecture (Ronneberger et al., 2015) and was developed for MR image contrast harmonization across protocol or scanner changes. For almost a decade, GANs (Goodfellow et al., 2014) have been the state of the art for image generation and image-to-image translation (Karras et al., 2021; Emami et al., 2020; Zhu et al., 2017; Isola et al., 2017). GANs such as (Dar et al., 2019; Liu et al., 2020; Luo et al., 2021; Peng et al., 2021) were created for multi-modal MR image synthesis, for instance T1- to T2-contrast. (Nie et al., 2017, 2018) performed cross-modal and cross-scanner image synthesis using GANs. Lately, DDPMs (Sohl-Dickstein et al., 2015; Ho et al., 2020) became the focus of attention. (Nichol and Dhariwal, 2021; Dhariwal and Nichol, 2021) further improved DDPMs, resulting in a transition of the state of the art for image generation from GANs to diffusion models. Their application includes text-to-image generation as in (Rombach et al., 2022; Saharia et al., 2022b), image-to-image translation (Saharia et al., 2022a; Seo et al., 2022; Wolleb et al., 2022c), inpainting (Saharia et al., 2022a; Lugmayr et al., 2022; Wolleb et al., 2022c) and deformable image registration (Kim et al., 2022). The recently introduced diffusion models are also used in medical image analysis. For instance for cross-modal (Lyu and Wang, 2022) and multi-modal MR image synthesis (Özbey et al., 2022), anomaly detection (Wolleb et al., 2022a) and synthetic image generation (Pinaya et al., 2022). In medical studies, processing of 3D data is often required. (Dorjsembe et al., 2022) showed the applicability of diffusion models to 3D data, but frequently, memory restrictions affect the processing of large volumes.

## 2. Method

DDPMs as described in (Nichol and Dhariwal, 2021) form the basis for the proposed method. They are a class of generative models based on an iterative noising process  $q$  and denoising process  $p_\theta$ . In the forward process  $q$ , Gaussian noise is added to an input image  $x$  for  $T$  time steps  $t$ . As the noise level is increased from a minimum at  $t = 0$  to a maximum at  $t = T$ , each image  $x_0, x_1, \dots, x_T$  displays a higher amount of noise compared to the previous one. The forward noising process  $q$  is defined as

$$q(x_t|x_{t-1}) := \mathcal{N}(x_t; \sqrt{1 - \beta_t}x_{t-1}, \beta_t\mathbf{I}), \quad (1)$$

where  $\mathbf{I}$  is the identity matrix and  $\beta_1, \dots, \beta_T$  are the forward process variances. With  $\alpha_t := 1 - \beta_t$  and  $\bar{\alpha}_t := \prod_{s=1}^t \alpha_s$  and using the reparametrization trick,  $x_t$  can be written as

$$x_t = \sqrt{\bar{\alpha}_t}x_0 + \sqrt{1 - \bar{\alpha}_t}\epsilon, \quad \text{with } \epsilon \sim \mathcal{N}(0, \mathbf{I}). \quad (2)$$

For the denoising process  $p_\theta$ , the aim is to reverse the forward process, hence to predict  $x_{t-1}$  from  $x_t$  for  $t \in \{T, \dots, 1\}$ . The learned model parameters  $\theta$  define the reverse process

$$p_\theta(x_{t-1}|x_t) := \mathcal{N}(x_{t-1}; \mu_\theta(x_t, t), \Sigma_\theta(x_t, t)). \quad (3)$$

To map images of the source contrast  $\mathcal{S}$  to the target contrast  $\mathcal{T}$ , we use the generative

process of DDPMs. We adapt the method of (Wolleb et al., 2022b), originally created for DDPM-based image segmentation using paired data, to translate an image  $B \in \mathcal{S}$  to  $B_{transformed}$ , which appears in the target contrast  $\mathcal{T}$ . The used data set provides for each of the  $m$  participants one 3D scan  $B$  of the source contrast  $\mathcal{S}$  and one corresponding 3D scan  $\hat{B}$  of the target contrast  $\mathcal{T}$ . Due to memory restrictions, we implement our model in 2D and slice each of the  $m$  scans of both contrasts into  $n$  slices and obtain for each participant  $B = \{b_i\}_{i=1}^n$  and  $\hat{B} = \{\hat{b}_i\}_{i=1}^n$  slices. We translate the slices  $\{b_i\}_{i=1}^n$  originating from a scan  $B \in \mathcal{S}$  such that they resemble the contrast of the slices  $\{\hat{b}_i\}_{i=1}^n$  originating from  $\hat{B} \in \mathcal{T}$ , whereby each baseline slice  $b_i$  has its corresponding ground truth  $\hat{b}_i$ . During training, depicted in Figure 2, we pick a random timestep  $t \in \{1, \dots, T\}$  and apply Equation 2 with  $x_0 = \hat{b}_i$  to compute a noisy image  $x_{b_i,t}$  from  $\hat{b}_i$ . Since we only want to change the scanner-related image

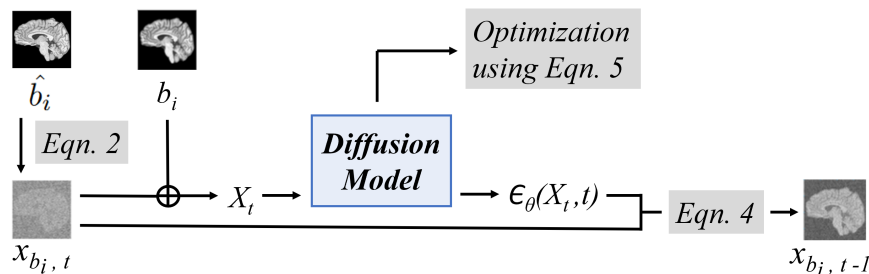


Figure 2: Overview of the training. Anatomical information is given through the concatenation of image  $b_i$  from  $B \in \mathcal{S}$  with noisy image  $x_{b_i,t}$ .  $X_t$  is used by the diffusion model to predict a slightly denoised image  $x_{b_i,t-1}$  from  $x_{b_i,t}$  using Equation 4.

contrast and not any anatomical features, we add anatomical information of our baseline image  $b_i$  through concatenation. We define the concatenated image as  $X_t := b_i \oplus x_{b_i,t}$  which serves as input for our diffusion model. We can compute  $x_{b_i,t-1}$  using Equation 4, which summarizes a denoising step as

$$x_{b_i,t-1} = \frac{1}{\sqrt{\alpha_t}} \left( x_{b_i,t} - \frac{1 - \alpha_t}{\sqrt{1 - \alpha_t}} \epsilon_\theta(X_t, t) \right) + \sigma_t \mathbf{z}, \quad \text{with } \mathbf{z} \sim \mathcal{N}(0, \mathbf{I}), \quad (4)$$

whereby  $\epsilon_\theta(X_t, t)$  is the output of the diffusion model at time step  $t$ ,  $\sigma_t$  describes the variance scheme and  $\mathbf{z}$  denotes the stochastic component of the process. The loss used to train the diffusion model  $\epsilon_\theta$  can be written as

$$\| \epsilon - \epsilon_\theta(X_t, t) \|^2 = \| \epsilon - \epsilon_\theta(b_i \oplus (\sqrt{\alpha_t} \hat{b}_i + \sqrt{(1 - \alpha_t)} \epsilon), t) \|^2, \quad \text{with } \epsilon \sim \mathcal{N}(0, \mathbf{I}). \quad (5)$$

For the two directions of the image mapping, 3T to 1.5T and 1.5T to 3T, two separate models need to be trained, as source and target contrast change. To translate a scan volume  $B = \{b_i\}_{i=1}^n \in \mathcal{S}$  to the target contrast  $\mathcal{T}$  during sampling, we translate every slice  $b_i$  to the synthetic slice  $x_{b_i,0}$  in the contrast of  $\mathcal{T}$ . Figure 3 summarizes the sampling process starting from  $x_{b_i,T} \sim \mathcal{N}(0, \mathbf{I})$ . The previously trained denoising model is now applied for every denoising step  $t \in \{T, \dots, 1\}$  using Equation 4. Anatomical information is also added

for every step  $t$  of the denoising process through the concatenation of  $b_i$  and  $x_{b_i,t}$ . We then stack the  $n$  output slices  $x_{b_i,0}$  to create our final 3D output volume  $B_{transformed} = \{x_{b_i,0}\}_{i=1}^n$ , displaying the whole brain in target contrast.

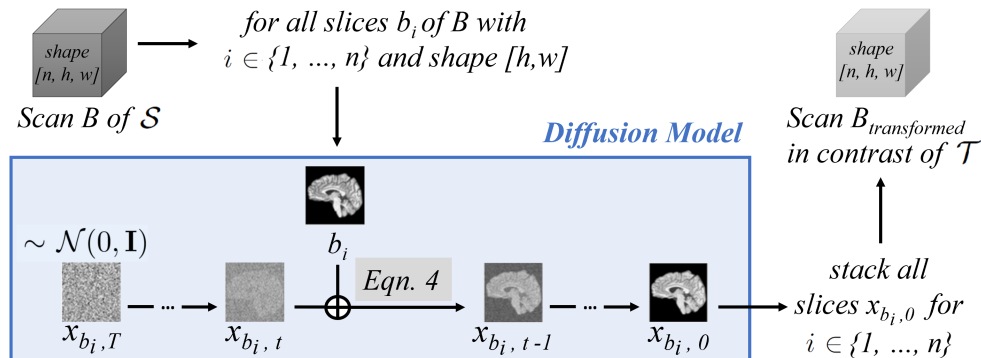


Figure 3: Translation from  $B \in \mathcal{S}$  to  $B_{transformed}$ . Each slice  $b_i$  of  $B \in \mathcal{S}$  is iteratively denoised by applying Equation 4 for steps  $t \in \{T, \dots, 1\}$ , whereby slice  $b_i$  is used to add anatomical information through concatenation. The 2D output slices  $\{x_{b_i,0}\}_{i=1}^n$  get stacked to  $B_{transformed}$ , showing the input scan  $B$  translated to  $\mathcal{T}$ .

### 3. Data Set and Training Details

We used a data set exclusively created to track a scanner change from a 1.5 T Siemens Magnetom Avanto to a 3 T Siemens Magnetom Skyra<sup>fit</sup> whole-body scanner in 2016 (Sinnecker et al., 2022). Scanner details can be found in Appendix A. The participants’ data is not public due to data privacy protection. Written consent was obtained from all participants. The data was coded (i.e., pseudoanonymized) at the time of the enrolment of the patients and includes scans of 22 healthy controls and 18 MS patients. All participants were scanned first in the 1.5 T scanner and after a median time interval of 3.5 months in the 3 T scanner. The relatively short time span between the scans ensures that no major disease progression happened in the MS patients, allowing a direct comparison of the scans and thereby forming a paired data set. Data set details can be found in Appendix B. Pre-processing of the original 3D data includes skull-stripping using HD-BET (Isensee et al., 2019), biasfield correction (Tustison et al., 2010), resampling of voxel spacing to  $1 \times 1 \times 1 \text{ mm}^3$  removal of the top and bottom 0.1 percentile of voxel intensities and normalization to voxel values between 0 and 1. With the ANTsPyx package, the paired images were registered based on affine and deformable transformation, using mutual information as similarity metric and an elastic regularization (Avants et al., 2014). We sliced each pre-processed 3D scan into 160 sagittal slices of shape  $[246, 262]$  that were then cropped to a size of  $[224, 224]$ . The cropping only affected background pixels. We trained our models for 300,000 iterations with a batch size of four on a NVIDIA GeForce RTX 2080 Ti GPU, taking about 60 hours. As in (Wolleb et al., 2022b), the number of channels in the first layer of the model is 128, and one attention head is used at resolution 16, resulting in 11,402,370 model parameters.

The learning rate used is  $10^{-4}$  for the Adam optimizer.  $T$  is set as 1000. Details on hyper-parameters and architecture can be found in (Nichol and Dhariwal, 2021). In addition to MSE calculation and histogram analysis, we evaluated CSF, GM and WM segmentations using FAST (Zhang et al., 2001) for the original images and the generated images. We did a four-fold cross-validation, combining data of healthy controls and MS patients in each fold. For each fold, the slices of 30 scans were used for training and those of 10 scans for testing.

#### 4. Results and Discussion

For the evaluation, we compare our diffusion model ( $DM$ ) with DeepHarmony ( $DH$ ) (Dewey et al., 2019) and  $pGAN$  (Dar et al., 2019). Implementation details of the comparing methods can be found in Appendix C. Each method takes an image  $B \in \mathcal{S}$  and generates the image  $B_{transformed}$  appearing in target contrast. The direct comparison of  $B$  versus  $\hat{B}$  is denoted as *Original*. All tables in this chapter show the average scores on the test set over a four-fold cross-validation, the variances are listed in Appendix D.

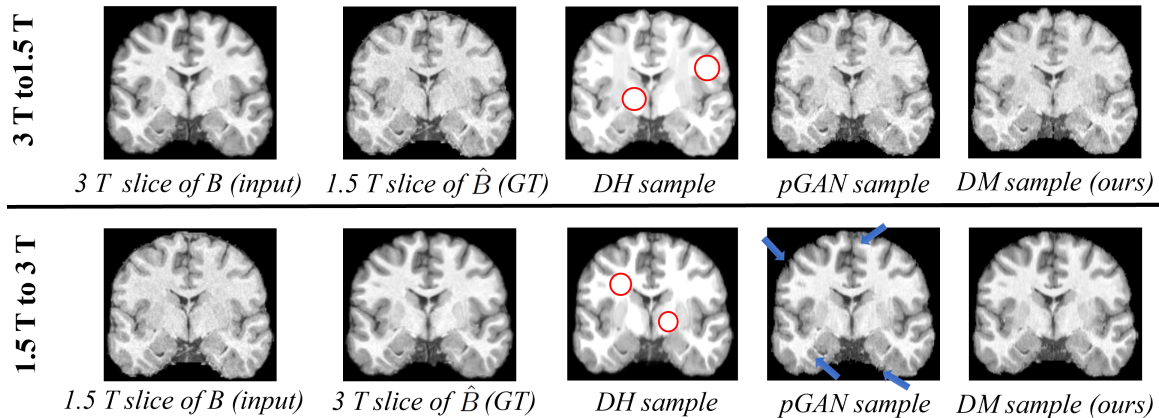


Figure 4: An exemplary coronal slice of a scan  $B \in \mathcal{S}$ , the corresponding ground truth (GT) slice of  $\hat{B} \in \mathcal{T}$  and slices of its mappings  $B_{transformed}$  in contrast  $\mathcal{T}$  generated by  $DH$ ,  $pGAN$  and our  $DM$  are shown for both mapping directions. The red circles indicate hyperintense regions generated by  $DH$ . The blue arrows point at stripe artifacts produced by  $pGAN$ . Further examples are provided in Appendix F.

Figure 4 contains examples of generated images and the corresponding input and ground truth slices. The original 1.5 T and 3 T images differ in contrast. While  $pGAN$  and our  $DM$  generate convincing mappings of the input images to target contrast,  $DH$  blurs the image and increases the brightness excessively for both directions of the image mapping. The examples shown are coronal slices from a 3D volume that was built by stacking sagittal slices. While images mapped to 3 T contrast by  $pGAN$  contain some stripe artifacts, mostly in the border regions of the brain, our  $DM$  does not create any stripe artifacts, indicating that processing the data in a slice-wise fashion is a valuable simplification.

To compare the different methods, we compute the Mean Squared Error (MSE) between

Table 1: MSE and AHD scores (formulas in Appendix D) for both directions of the mapping.

Method	3 T to 1.5 T		1.5 T to 3 T	
	MSE	AHD	MSE	AHD
<i>Original</i>	$1.85 \times 10^{-3}$	$6.15 \times 10^5$	$1.85 \times 10^{-3}$	$6.15 \times 10^5$
<i>DH</i>	$2.30 \times 10^{-3}$	$7.49 \times 10^5$	$1.73 \times 10^{-3}$	$8.22 \times 10^5$
<i>pGAN</i>	<b><math>1.50 \times 10^{-3}</math></b>	<b><math>1.27 \times 10^5</math></b>	$0.94 \times 10^{-3}$	$2.07 \times 10^5$
<i>DM (ours)</i>	$1.61 \times 10^{-3}$	$1.31 \times 10^5$	<b><math>0.76 \times 10^{-3}</math></b>	<b><math>1.48 \times 10^5</math></b>

the ground truth images  $\hat{B}$  and the translated images  $B_{transformed}$ . In Table 1 we report the MSE as well as the sum of the bin-wise absolute difference between the histograms (AHD), whereby each histogram consists of 255 bins. Mapping images of 3 T to 1.5 T contrast, our *DM* and the *pGAN* manage to decrease the MSE and to improve the AHD compared to *Original*. *DH* cannot compete and produces a higher MSE and AHD than the *Original*. Mapping 1.5 T to 3 T contrast, our *DM* outperforms *Original*, *DH* and *pGAN* regarding MSE and AHD. The results show that the contrast harmonization shifts the voxel distributions characteristic for  $\mathcal{S}$  towards the distributions of  $\mathcal{T}$ . For both directions of the mapping, exemplary histograms can be found in Appendix E. The histograms of the samples generated by *pGAN* and our *DM* better align with the histogram of the ground truth  $\hat{B} \in \mathcal{T}$  than the histogram of  $B \in \mathcal{S}$ , for both directions of the mapping.

Table 2: Absolute volume differences in  $\text{mm}^3$  of the segmentations of CSF, GM and WM of all original images  $B \in \mathcal{S}$  and generated images  $B_{transformed}$  compared to ground truths  $\hat{B} \in \mathcal{T}$  for both directions of the mapping. The best result per class is bold.

Method	3 T to 1.5 T			1.5 T to 3 T		
	CSF	GM	WM	CSF	GM	WM
<i>Original</i>	$3.72 \times 10^4$	$9.32 \times 10^4$	$8.88 \times 10^4$	$3.72 \times 10^4$	$9.32 \times 10^4$	$8.88 \times 10^4$
<i>pGAN</i>	<b><math>1.12 \times 10^4</math></b>	<b><math>1.14 \times 10^4</math></b>	$1.91 \times 10^4$	$3.11 \times 10^4$	$6.15 \times 10^4$	$2.09 \times 10^4$
<i>DM (ours)</i>	$1.95 \times 10^4$	$1.54 \times 10^4$	<b><math>1.59 \times 10^4</math></b>	<b><math>1.79 \times 10^4</math></b>	<b><math>3.91 \times 10^4</math></b>	<b><math>1.49 \times 10^4</math></b>

To obtain further insight about the increased comparability of  $B_{transformed}$  with  $\hat{B} \in \mathcal{T}$  for downstream tasks, we segmented the original 3D images as well as the 3D images generated by our *DM* and *pGAN* into the three classes CSF, GM and WM using FAST (Zhang et al., 2001). *DH* could not be considered for this comparison, as the quality of the generated images was not high enough to create meaningful segmentations using FAST. Examples of the segmentations can be found in Appendix G. As the voxel size is  $1 \times 1 \times 1 \text{ mm}^3$ , we calculate the volume of each class by counting the voxels attributed to each class. For both directions of the image mapping we then compute the volume differences for each class between the ground truth segmentation of  $\hat{B}$  and the segmentations of  $B$  or  $B_{transformed}$ , respectively. Table 2 shows that *pGAN* and our *DM* decrease the differences between

the segmentation volumes of  $B_{transformed}$  and  $\hat{B}$  compared to the segmentation volume difference between  $B$  and  $\hat{B}$  for both directions of the mapping.  $pGAN$  and our  $DM$  show similar performance for the mapping from 3 T to 1.5 T but our model performs better for the mapping from 1.5 T to 3 T. We conclude that harmonizing contrasts before segmenting allows more coherent assignment of voxels to classes, enabling better comparison of tissue volumes between scans. We use the Dice score and the Hausdorff distance (HD) to assess that the contrast harmonization did not negatively affect the location of the segmented volumes, whereby the ground truth is given by the segmentation of  $\hat{B}$ . Table 3 shows that our  $DM$  achieves better HD scores than  $pGAN$  and the *Original* for all classes. The Dice scores for our  $DM$  remain in the ranges of the *Original* for the mapping from 3 T to 1.5 T. For the mapping from 1.5 T to 3 T, however, our  $DM$  improves the Dice scores of GM and WM considerably compared to the *Original*. According to Tables 1 and 2,  $pGAN$  performed better than our  $DM$  for the mapping from 3 T to 1.5 T, but regarding the HD, our  $DM$  seems more reliable for both directions of the mapping. The results indicate that using our  $DM$ , the contrast harmonization and the resulting change in voxel distribution and segmentation volumes occurs at the desired regions.

Table 3: Dice scores and HD of the segmentations of CSF, GM and WM of all original images  $B \in \mathcal{S}$  and generated images  $B_{transformed}$  compared to the ground truth segmentations of  $\hat{B} \in \mathcal{T}$  for both directions of the mapping. The best result per class is bold.

Method	3 T to 1.5 T						1.5 T to 3 T					
	Dice			HD			Dice			HD		
	CSF	GM	WM	CSF	GM	WM	CSF	GM	WM	CSF	GM	WM
<i>Original</i>	0.82	<b>0.82</b>	0.87	10.21	8.68	11.16	<b>0.82</b>	0.82	0.87	10.21	8.68	11.16
$pGAN$	<b>0.82</b>	0.79	0.87	21.48	13.54	12.14	0.76	0.85	0.92	8.67	7.24	9.48
$DM$ (ours)	0.80	0.79	<b>0.88</b>	<b>9.11</b>	<b>6.73</b>	<b>7.67</b>	0.81	<b>0.88</b>	<b>0.92</b>	<b>8.65</b>	<b>7.01</b>	<b>9.30</b>

## 5. Conclusion

We present a novel method for contrast harmonization based on DDPMs. Using paired data from a source contrast  $\mathcal{S}$  and a target contrast  $\mathcal{T}$ , our method allows us to translate a scan  $B$  of the source contrast  $\mathcal{S}$  to scan  $B_{transformed}$  appearing in the contrast of  $\mathcal{T}$ . For the image-to-image translation, our diffusion model receives information from the source image  $B$ , as we only want to adjust the contrast while keeping the anatomical information. The translation improves comparability between scans from different contrasts for further evaluation and downstream tasks such as tissue segmentation. Our model outperforms the comparing methods for the mapping from 1.5 T to 3 T and generates great results for the opposite image mapping. Compared to GANs, diffusion models are not trained in an adversarial manner, making the training straightforward. The input and output of our model are 2D slices, allowing us to save memory compared to models trained on 3D volumes. Stacking the 2D images to a 3D volume does not generate any stripe artifacts,



showing us that our method only changes the contrast and not the anatomical structure. Due to the image generation characteristics of DDPMs, our method has a long sampling time compared to the other methods, which could be improved by using other sampling schemes (Song et al., 2020). So far, our model was only trained on skull-stripped data sets, limiting a more in-depth temporal analysis of brain-volume changes. As our next step, we will omit the skull-stripping during pre-processing, enabling observing brain-volume changes relative to the fixed skull size.

### **Acknowledgments**

This project was partially funded by the Research Fund for Junior Researchers of the University of Basel.

## References

- Brian B Avants, Nicholas J Tustison, Michael Stauffer, Gang Song, Baohua Wu, and James C Gee. The insight toolkit image registration framework. *Frontiers in neuroinformatics*, 8:44, 2014.
- Ahmed Ba-Ssalamah, Iris M Nöbauer-Huhmann, Katja Pinker, Nadja Schibany, Rupert Prokesch, Sheida Mehrain, Vladimir Mlynárik, Amura Fog, Karl Heimberger, and Siegfried Trattnig. Effect of contrast dose and field strength in the magnetic resonance detection of brain metastases. *Investigative radiology*, 38(7):415–422, 2003.
- Mahsa Dadar, Simon Duchesne, CCNA Group, et al. Reliability assessment of tissue classification algorithms for multi-center and multi-scanner data. *NeuroImage*, 217:116928, 2020.
- Salman UH Dar, Mahmut Yurt, Levent Karacan, Aykut Erdem, Erkut Erdem, and Tolga Cukur. Image synthesis in multi-contrast mri with conditional generative adversarial networks. *IEEE transactions on medical imaging*, 38(10):2375–2388, 2019.
- Blake E Dewey, Can Zhao, Jacob C Reinhold, Aaron Carass, Kathryn C Fitzgerald, Elias S Sotirchos, Shiv Saidha, Jiwon Oh, Dzung L Pham, Peter A Calabresi, et al. Deepharmony: A deep learning approach to contrast harmonization across scanner changes. *Magnetic resonance imaging*, 64:160–170, 2019.
- Prafulla Dhariwal and Alexander Nichol. Diffusion models beat gans on image synthesis. *Advances in Neural Information Processing Systems*, 34:8780–8794, 2021.
- Giulio Disanto, Pascal Benkert, Johannes Lorscheider, Stefanie Mueller, Jochen Vehoff, Chiara Zecca, Simon Ramseier, Lutz Achtnichts, Oliver Findling, Krassen Nedeltchev, et al. The swiss multiple sclerosis cohort-study (smc): a prospective swiss wide investigation of key phases in disease evolution and new treatment options. *PloS one*, 11(3): e0152347, 2016.
- Zolnamar Dorjsembe, Sodontavilan Odonchimed, and Furen Xiao. Three-dimensional medical image synthesis with denoising diffusion probabilistic models. In *Medical Imaging with Deep Learning*. PMLR, 2022.
- Hajar Emami, Majid Moradi Aliabadi, Ming Dong, and Ratna Babu Chinnam. Spa-gan: Spatial attention gan for image-to-image translation. *IEEE Transactions on Multimedia*, 23:391–401, 2020.
- Ian Goodfellow, Jean Pouget-Abadie, Mehdi Mirza, Bing Xu, David Warde-Farley, Sherjil Ozair, Aaron Courville, and Yoshua Bengio. Generative adversarial nets. In Z. Ghahramani, M. Welling, C. Cortes, N. Lawrence, and K.Q. Weinberger, editors, *Advances in Neural Information Processing Systems*, volume 27. Curran Associates, Inc., 2014.
- Jonathan Ho, Ajay Jain, and Pieter Abbeel. Denoising diffusion probabilistic models. *Advances in Neural Information Processing Systems*, 33:6840–6851, 2020.

- Fabian Isensee, Marianne Schell, Irada Pflueger, Gianluca Brugnara, David Bonekamp, Ulf Neuberger, Antje Wick, Heinz-Peter Schlemmer, Sabine Heiland, Wolfgang Wick, et al. Automated brain extraction of multisequence mri using artificial neural networks. *Human brain mapping*, 40(17):4952–4964, 2019.
- Phillip Isola, Jun-Yan Zhu, Tinghui Zhou, and Alexei A Efros. Image-to-image translation with conditional adversarial networks. In *Proceedings of the IEEE conference on computer vision and pattern recognition*, pages 1125–1134, 2017.
- Tero Karras, Miika Aittala, Samuli Laine, Erik Härkönen, Janne Hellsten, Jaakko Lehtinen, and Timo Aila. Alias-free generative adversarial networks. *Advances in Neural Information Processing Systems*, 34:852–863, 2021.
- Shiva Keihaninejad, Rolf A Heckemann, Gianlorenzo Fagiolo, Mark R Symms, Joseph V Hajnal, Alexander Hammers, Alzheimer’s Disease Neuroimaging Initiative, et al. A robust method to estimate the intracranial volume across mri field strengths (1.5 t and 3t). *Neuroimage*, 50(4):1427–1437, 2010.
- Boah Kim, Inhwa Han, and Jong Chul Ye. Diffusemorph: Unsupervised deformable image registration using diffusion model. In *European Conference on Computer Vision*, pages 347–364. Springer, 2022.
- Julia Krüger, Roland Opfer, Nils Gessert, Ann-Christin Ostwaldt, Praveena Manogaran, Hagen H Kitzler, Alexander Schlaefer, and Sven Schippling. Fully automated longitudinal segmentation of new or enlarged multiple sclerosis lesions using 3d convolutional neural networks. *NeuroImage: Clinical*, 28:102445, 2020.
- Hyunwoo Lee, Kunio Nakamura, Sridar Narayanan, Robert A Brown, Douglas L Arnold, Alzheimer’s Disease Neuroimaging Initiative, et al. Estimating and accounting for the effect of mri scanner changes on longitudinal whole-brain volume change measurements. *Neuroimage*, 184:555–565, 2019.
- Xiaoming Liu, Aihui Yu, Xiangkai Wei, Zhifang Pan, and Jinshan Tang. Multimodal mr image synthesis using gradient prior and adversarial learning. *IEEE Journal of Selected Topics in Signal Processing*, 14(6):1176–1188, 2020.
- Andreas Lugmayr, Martin Danelljan, Andres Romero, Fisher Yu, Radu Timofte, and Luc Van Gool. Repaint: Inpainting using denoising diffusion probabilistic models. In *Proceedings of the IEEE/CVF Conference on Computer Vision and Pattern Recognition*, pages 11461–11471, 2022.
- Yanmei Luo, Dong Nie, Bo Zhan, Zhiang Li, Xi Wu, Jiliu Zhou, Yan Wang, and Dinggang Shen. Edge-preserving mri image synthesis via adversarial network with iterative multi-scale fusion. *Neurocomputing*, 452:63–77, 2021.
- Qing Lyu and Ge Wang. Conversion between ct and mri images using diffusion and score-matching models. *arXiv preprint arXiv:2209.12104*, 2022.
- Don H Mahad, Bruce D Trapp, and Hans Lassmann. Pathological mechanisms in progressive multiple sclerosis. *The Lancet Neurology*, 14(2):183–193, 2015.

- Antoine J Maubon, Jean-Michel Ferru, Vincent Berger, Marie Colette Soulage, Marc De-Graef, Pierre Aubas, Patrice Coupeau, Erik Dumont, and Jean-Pierre Rouanet. Effect of field strength on mr images: comparison of the same subject at 0.5, 1.0, and 1.5 t. *Radiographics*, 19(4):1057–1067, 1999.
- Alexander Quinn Nichol and Prafulla Dhariwal. Improved denoising diffusion probabilistic models. In *International Conference on Machine Learning*, pages 8162–8171. PMLR, 2021.
- Dong Nie, Roger Trullo, Jun Lian, Caroline Petitjean, Su Ruan, Qian Wang, and Dinggang Shen. Medical image synthesis with context-aware generative adversarial networks. In *International conference on medical image computing and computer-assisted intervention*, pages 417–425. Springer, 2017.
- Dong Nie, Roger Trullo, Jun Lian, Li Wang, Caroline Petitjean, Su Ruan, Qian Wang, and Dinggang Shen. Medical image synthesis with deep convolutional adversarial networks. *IEEE Transactions on Biomedical Engineering*, 65(12):2720–2730, 2018.
- Muzaffer Özbey, Salman UH Dar, Hasan A Bedel, Onat Dalmaz, Şaban Öztürk, Alper Güngör, and Tolga Çukur. Unsupervised medical image translation with adversarial diffusion models. *arXiv preprint arXiv:2207.08208*, 2022.
- Bo Peng, Bingzheng Liu, Yi Bin, Lili Shen, and Jianjun Lei. Multi-modality mr image synthesis via confidence-guided aggregation and cross-modality refinement. *IEEE Journal of Biomedical and Health Informatics*, 26(1):27–35, 2021.
- Walter HL Pinaya, Petru-Daniel Tudosiu, Jessica Dafflon, Pedro F Da Costa, Virginia Fernandez, Parashkev Nachev, Sebastien Ourselin, and M Jorge Cardoso. Brain imaging generation with latent diffusion models. In *MICCAI Workshop on Deep Generative Models*, pages 117–126. Springer, 2022.
- Robin Rombach, Andreas Blattmann, Dominik Lorenz, Patrick Esser, and Björn Ommer. High-resolution image synthesis with latent diffusion models. In *Proceedings of the IEEE/CVF Conference on Computer Vision and Pattern Recognition*, pages 10684–10695, 2022.
- Olaf Ronneberger, Philipp Fischer, and Thomas Brox. U-net: Convolutional networks for biomedical image segmentation. In *International Conference on Medical image computing and computer-assisted intervention*, pages 234–241. Springer, 2015.
- Chitwan Saharia, William Chan, Huiwen Chang, Chris Lee, Jonathan Ho, Tim Salimans, David Fleet, and Mohammad Norouzi. Palette: Image-to-image diffusion models. In *ACM SIGGRAPH 2022 Conference Proceedings*, pages 1–10, 2022a.
- Chitwan Saharia, William Chan, Saurabh Saxena, Lala Li, Jay Whang, Emily Denton, Seyed Kamyar Seyed Ghasemipour, Burcu Karagol Ayan, S Sara Mahdavi, Rapha Gontijo Lopes, et al. Photorealistic text-to-image diffusion models with deep language understanding. *arXiv preprint arXiv:2205.11487*, 2022b.

- Junyoung Seo, Gyuseong Lee, Seokju Cho, Jiyoung Lee, and Seungryong Kim. Midms: Matching interleaved diffusion models for exemplar-based image translation. *arXiv preprint arXiv:2209.11047*, 2022.
- Tim Sinnecker, Sabine Schädelin, Pascal Benkert, Esther Ruberte, Michael Amann, Johanna M Lieb, Yvonne Naegelin, Jannis Müller, Jens Kuhle, Tobias Derfuss, et al. Brain atrophy measurement over a mri scanner change in multiple sclerosis. *NeuroImage: Clinical*, 36:103148, 2022.
- Stephen M Smith, Yongyue Zhang, Mark Jenkinson, Jacqueline Chen, Paul M Matthews, Antonio Federico, and Nicola De Stefano. Accurate, robust, and automated longitudinal and cross-sectional brain change analysis. *Neuroimage*, 17(1):479–489, 2002.
- Stephen M Smith, Mark Jenkinson, Mark W Woolrich, Christian F Beckmann, Timothy EJ Behrens, Heidi Johansen-Berg, and PM Matthews. Advances in functional and structural mr image analysis and implementation as fsl technical report tr04ss2. *Neuroimage*, 23(S1):208–219, 2004.
- Jascha Sohl-Dickstein, Eric Weiss, Niru Maheswaranathan, and Surya Ganguli. Deep unsupervised learning using nonequilibrium thermodynamics. In *International Conference on Machine Learning*, pages 2256–2265. PMLR, 2015.
- Jiaming Song, Chenlin Meng, and Stefano Ermon. Denoising diffusion implicit models. *arXiv preprint arXiv:2010.02502*, 2020.
- Nicholas J Tustison, Brian B Avants, Philip A Cook, Yuanjie Zheng, Alexander Egan, Paul A Yushkevich, and James C Gee. N4itk: improved n3 bias correction. *IEEE transactions on medical imaging*, 29(6):1310–1320, 2010.
- Julia Wolleb, Florentin Bieder, Robin Sandkühler, and Philippe C. Cattin. Diffusion models for medical anomaly detection. In *International Conference on Medical image computing and computer-assisted intervention*, page 35–45. Springer, 2022a.
- Julia Wolleb, Robin Sandkuehler, Florentin Bieder, Philippe Valmaggia, and Philippe C. Cattin. Diffusion models for implicit image segmentation ensembles. In *Medical Imaging with Deep Learning*, pages 1336–1348. PMLR, 2022b.
- Julia Wolleb, Robin Sandkühler, Florentin Bieder, and Philippe C Cattin. The swiss army knife for image-to-image translation: Multi-task diffusion models. *arXiv preprint arXiv:2204.02641*, 2022c.
- Yongyue Zhang, Michael Brady, and Stephen Smith. Segmentation of brain mr images through a hidden markov random field model and the expectation-maximization algorithm. *IEEE transactions on medical imaging*, 20(1):45–57, 2001.
- Jun-Yan Zhu, Taesung Park, Phillip Isola, and Alexei A Efros. Unpaired image-to-image translation using cycle-consistent adversarial networks. In *Proceedings of the IEEE international conference on computer vision*, pages 2223–2232, 2017.

## Appendix A. Scanner Details

Table 4: MR Scanners used for the data acquisition ([Sinnecker et al., 2022](#))

	<b>Previous Scanner</b>	<b>Current Scanner</b>
Manufacturer	Siemens Healthineers Erlangen, Germany	Siemens Healthineers Erlangen, Germany
Model Name	Magnetom Avanto	Magnetom Skyra <sup>fit</sup>
Magnetic Field Strength	1.5 T	3 T
Repetition Time	2080 <i>ms</i>	2300 <i>ms</i>
Inversion Time	1100 <i>ms</i>	900 <i>ms</i>
Echo Time	3.1 <i>ms</i>	2.94 <i>ms</i>
Imaging Matrix	240 x 256	240 x 256
Field of View (FOV)	234 x 250 mm <sup>2</sup>	240 x 256 mm <sup>2</sup>
Pixel Bandwidth	130 <i>Hz</i> per Pixel	240 <i>Hz</i> per Pixel
Flip Angle	15 <i>degrees</i>	9 <i>degrees</i>
Scanner Image Filter	Prescan-Normalization	Prescan-Normalization and Distortion Correction in 3D
Software Version	syngo MR B17	syngo MR VE11C
Sequence used for Data Set	MPRAGE	MPRAGE
Scan Period	2012 - 2016	2016 - present

## Appendix B. Data Set Details

The MS patients are part of a longitudinal MS study ([Disanto et al., 2016](#)). Both, MS patients and healthy controls were scanned first in the 1.5 T scanner and after the scanner change in the 3 T scanner (median time interval 3.5 months, range 1.7 – 5.2 months).

Table 5: Details about the participants included in the data set, provided by ([Sinnecker et al., 2022](#))

	<b>Multiple Sclerosis</b>	<b>Healthy Controls</b>
Number of Female Participants	14	11
Number of Male Participants	4	11
Age in Years, Mean [SD]	51.7 [ $\pm 12.7$ ]	28.9 [ $\pm 7.6$ ]

## Appendix C. Implementation Details

We compared our models against *DeepHarmony* (*DH*) and *pGAN*. For both comparing methods, we used the same four train and test folds as for our model to perform cross-validation.

Implementation details:

- *DH*: to make it more comparable to our method, we used 2D sagittal slices with shape [256, 256] as input, instead of the 2.5 dimensional implementation proposed in the paper. We cropped the output to [224, 224] and stacked the slices to a 3D volume of shape [160, 224, 224]. We trained the model for 300 epochs. We used a batch size of eight as in the original implementation and adjusted the learning rate to  $10^{-4}$  as the original learning rate was not compatible with our images. For further implementation details refer to (Dewey et al., 2019).
- *pGAN*: we trained the models for 300 epochs (150 with normal learning rate, 150 with the learning rate decayed to zero) with a batch size of four. We used no neighbouring slices. The cycle loss weight as well as the perceptual loss weight were set to 100. The processed slices were of shape [256, 256], we cropped and stacked the output slices to shape [160, 224, 224] for comparison with our model. For further implementation details refer to (Dar et al., 2019) and <https://github.com/icon-lab/pGAN-cGAN>.

## Appendix D. Detailed Metrics

The MSE was calculated using

$$MSE = \sum_{i=1}^N (a_i - b_i)^2 \quad (6)$$

with  $a$  and  $b$  being the images to compare and  $i$  iterating over all voxels  $N$ . The squared differences are summed. To calculate the AHD we used the following formula

$$AHD = \sum_{i=1}^{bins} |h_1(x_i) - h_2(x_i)| \quad (7)$$

with  $h_1$  and  $h_2$  being the histograms to compare for all bins  $x_i$ , with  $i$  ranging from one to the total number of bins.

Table 6: MSE and AHD averages including variances over four-fold cross-validation for the mapping from 3 T to 1.5 T contrast.

Method	MSE	AHD
Original	$1.85[\pm 0.03] \times 10^{-3}$	$6.15[\pm 0.12] \times 10^5$
DH	$2.30[\pm 0.07] \times 10^{-3}$	$7.49[\pm 0.09] \times 10^5$
pGAN	<b><math>1.50[\pm 0.03] \times 10^{-3}</math></b>	<b><math>1.27[\pm 0.07] \times 10^5</math></b>
DM (ours)	$1.61[\pm 0.03] \times 10^{-3}$	$1.31[\pm 0.16] \times 10^5$

Table 7: MSE and AHD averages including variances over four-fold cross-validation for the mapping from 1.5 T to 3 T contrast.

Method	MSE	AHD
Original	$1.85[\pm 0.03] \times 10^{-3}$	$6.15[\pm 0.12] \times 10^5$
DH	$1.73[\pm 0.07] \times 10^{-3}$	$8.22[\pm 0.14] \times 10^5$
pGAN	$0.94[\pm 0.11] \times 10^{-3}$	$2.07[\pm 0.34] \times 10^5$
DM (ours)	<b><math>0.76[\pm 0.008] \times 10^{-3}</math></b>	<b><math>1.48[\pm 0.16] \times 10^5</math></b>



Table 8: Average CSF, GM and WM segmentation differences and variances of the four-fold cross-validation. Differences between  $\hat{B}$  and  $B$  as well as between  $\hat{B}$  and  $B_{transformed}$  for the mapping from 3 T to 1.5 T contrast.

Method	CSF	GM	WM
Original	$3.72[\pm 0.43] \times 10^4$	$9.32[\pm 0.93] \times 10^4$	$8.88[\pm 0.58] \times 10^4$
pGAN	<b><math>1.12[\pm 0.17] \times 10^4</math></b>	<b><math>1.41[\pm 0.23] \times 10^4</math></b>	$1.91[\pm 0.19] \times 10^4$
DM (ours)	$1.95[\pm 0.24] \times 10^4$	$1.54[\pm 0.40] \times 10^4$	<b><math>1.59[\pm 0.24] \times 10^4</math></b>

Table 9: Average CSF, GM and WM segmentation differences and variances of the four-fold cross-validation. Differences between  $\hat{B}$  and  $B$  as well as between  $\hat{B}$  and  $B_{transformed}$  for the mapping from 1.5 T to 3 T contrast.

Method	CSF	GM	WM
Original	$3.72[\pm 0.43] \times 10^4$	$9.32[\pm 0.93] \times 10^4$	$8.88[\pm 0.58] \times 10^4$
pGAN	$3.11[\pm 0.55] \times 10^4$	$6.15[\pm 0.51] \times 10^4$	$2.10[\pm 0.27] \times 10^4$
DM (ours)	<b><math>1.79[\pm 0.06] \times 10^4</math></b>	<b><math>3.91[\pm 0.19] \times 10^4</math></b>	<b><math>1.49[\pm 0.65] \times 10^4</math></b>

Table 10: Average Dice scores and variances of the four-fold cross-validation of segmentations of CSF, GM and WM of  $B$  and of  $B_{transformed}$  compared to ground truth segmentation of  $\hat{B}$  for the mapping from 3 T to 1.5 T contrast.

Method	CSF	GM	WM
Original	0.8188 $[\pm 0.0095]$	<b>0.8180<math>[\pm 0.0041]</math></b>	0.8715 $[\pm 0.0031]$
pGAN	<b>0.8205<math>[\pm 0.0075]</math></b>	0.7925 $[\pm 0.0040]$	0.8745 $[\pm 0.0029]$
DM (ours)	0.7980 $[\pm 0.0052]$	0.7918 $[\pm 0.0029]$	<b>0.8762<math>[\pm 0.0027]</math></b>

Table 11: Average Dice scores and variances of the four-fold cross-validation of segmentations of CSF, GM and WM of  $B$  and of  $B_{transformed}$  compared to ground truth segmentation of  $\hat{B}$  for the mapping from 1.5 T to 3 T contrast.

Method	CSF	GM	WM
Original	<b>0.8188<math>[\pm 0.0095]</math></b>	0.8180 $[\pm 0.0041]$	0.8715 $[\pm 0.0031]$
pGAN	0.7607 $[\pm 0.0113]$	0.8521 $[\pm 0.0049]$	0.9163 $[\pm 0.0034]$
DM (ours)	0.8094 $[\pm 0.0101]$	<b>0.8760<math>[\pm 0.0045]</math></b>	<b>0.9232<math>[\pm 0.0031]</math></b>

Table 12: Average Hausdorff distances and variances of the four-fold cross validation of segmentations of CSF, GM and WM of  $B$  and of  $B_{transformed}$  compared to ground truth segmentation of  $\hat{B}$  for the mapping from 3 T to 1.5 T contrast.

<b>Method</b>	<b>CSF</b>	<b>GM</b>	<b>WM</b>
Original	10.21[±1.03]	8.68[±0.83]	11.16[±0.99]
pGAN	21.48[±5.88]	13.54[±3.53]	12.14[±2.98]
DM (ours)	<b>9.11[±1.05]</b>	<b>6.73[±1.02]</b>	<b>7.67[±1.02]</b>

Table 13: Average Hausdorff distances and variances of the four-fold cross validation of segmentations of CSF, GM and WM of  $B$  and of  $B_{transformed}$  compared to ground truth segmentation of  $\hat{B}$  for the mapping from 1.5 T to 3 T contrast.

<b>Method</b>	<b>CSF</b>	<b>GM</b>	<b>WM</b>
Original	10.21[±1.03]	8.68[±0.83]	11.16[±0.99]
pGAN	8.67[±0.80]	7.24[±0.90]	9.48[±1.04]
DM (ours)	<b>8.65[±0.91]</b>	<b>7.01[±0.81]</b>	<b>9.30[±1.33]</b>

### Appendix E. Histogram Examples

In Figures 5, 6, 7 and 8 we show exemplary histograms of both, healthy control and MS patient scans for both directions of the image mapping. Each histogram consists of 255 bins. Each figure contains the histograms of  $B$ ,  $\hat{B}$  and the generated volumes  $B_{transformed}$ . The histograms of  $DH$  are shifted towards the brightest voxels for both directions of the mapping. Due to this comparatively high amount of white voxels, the histograms of the  $DH$  samples are cropped in Figures 5 - 8. The initial 1.5 T and 3 T histograms show big differences. Both show two peaks, but for the 3 T images, these are further apart, letting us perceive images of higher contrast compared to the 1.5 T images. In Figures 5 - 8, our  $DM$  and  $pGAN$  manage to align the histograms of the generated samples much closer with these of the ground truths  $\hat{B} \in \mathcal{T}$  than the initial histograms of  $B \in \mathcal{S}$ . Therefore we assume that for both methods, the contrast harmonization is proving effective, for healthy control as well as for MS patient scans.

**Histograms of a Healthy Control 3 T to 1.5 T**

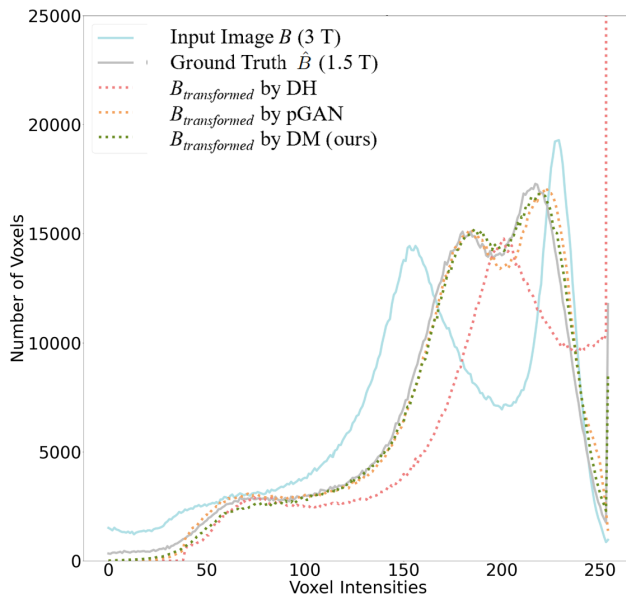


Figure 5: Exemplary histograms of one healthy control for the mapping from 3 T to 1.5 T. The histograms of  $B_{transformed}$  generated by  $pGAN$  and our  $DM$  align the ground truth histogram of  $\hat{B}$  well compared to the histogram of the input image  $B$ .

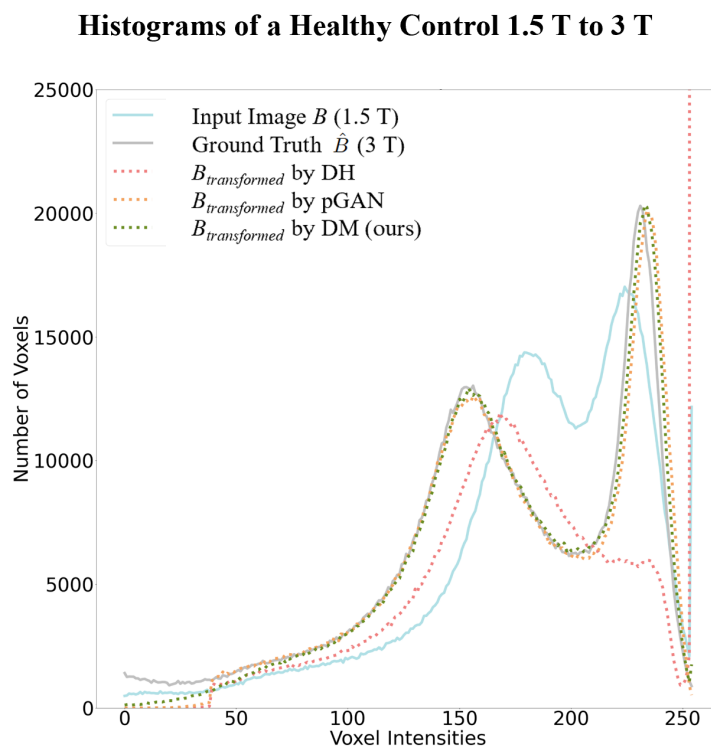


Figure 6: Exemplary histograms of one healthy control for the mapping from 1.5 T to 3 T. The histograms of  $B_{transformed}$  generated by  $pGAN$  and our  $DM$  align the ground truth histogram of  $\hat{B}$  well compared to the histogram of the input image  $B$ .

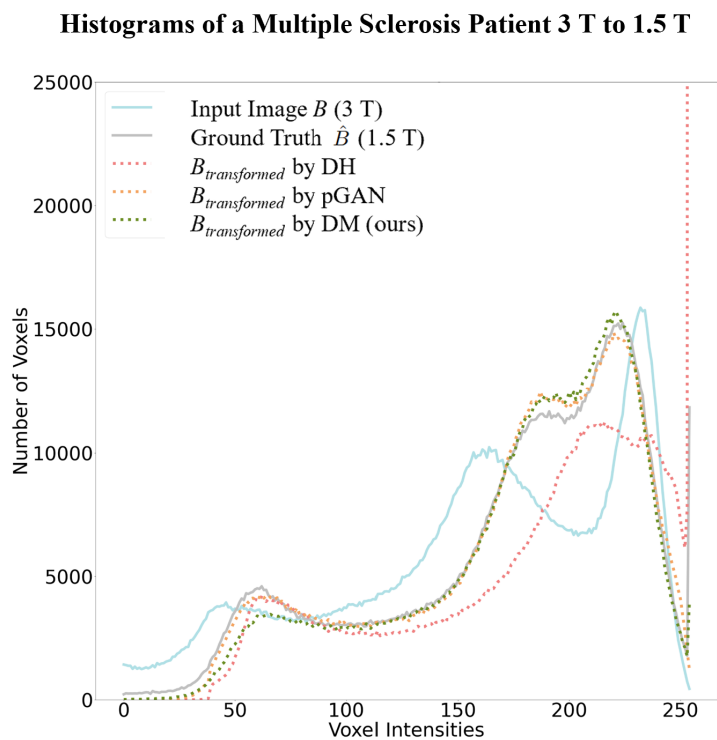


Figure 7: Exemplary histograms of one MS patient for the mapping from 3 T to 1.5 T. The histograms of  $B_{transformed}$  generated by  $pGAN$  and our  $DM$  align the ground truth histogram of  $\hat{B}$  well compared to the histogram of the input image  $B$ .

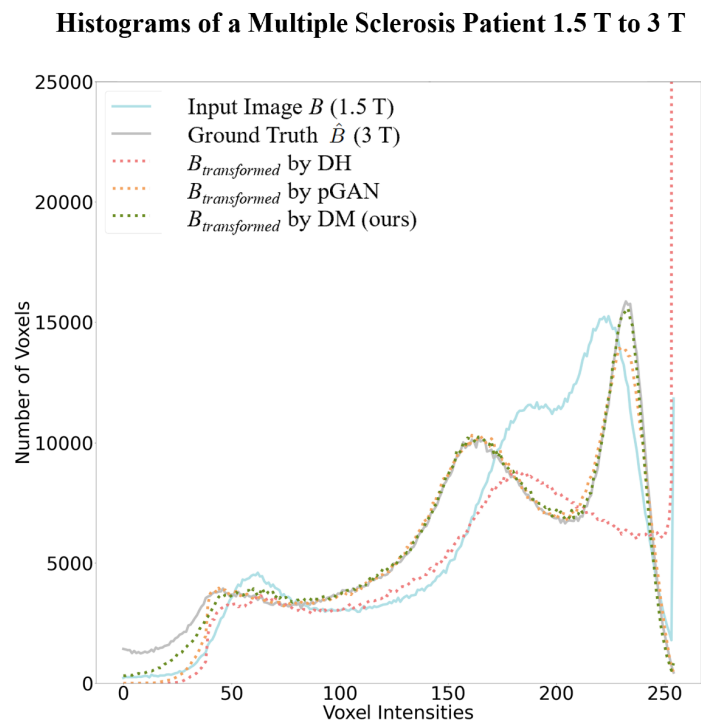


Figure 8: Exemplary histograms of one MS patient for the mapping from 1.5 T to 3 T. The histogram of  $B_{transformed}$  generated by  $pGAN$  aligns the ground truth histogram of  $\hat{B}$  well compared to the histogram of the input image  $B$ , while our  $DM$  manages to almost perfectly match the peaks of  $\hat{B}$ .

## Appendix F. Image Examples

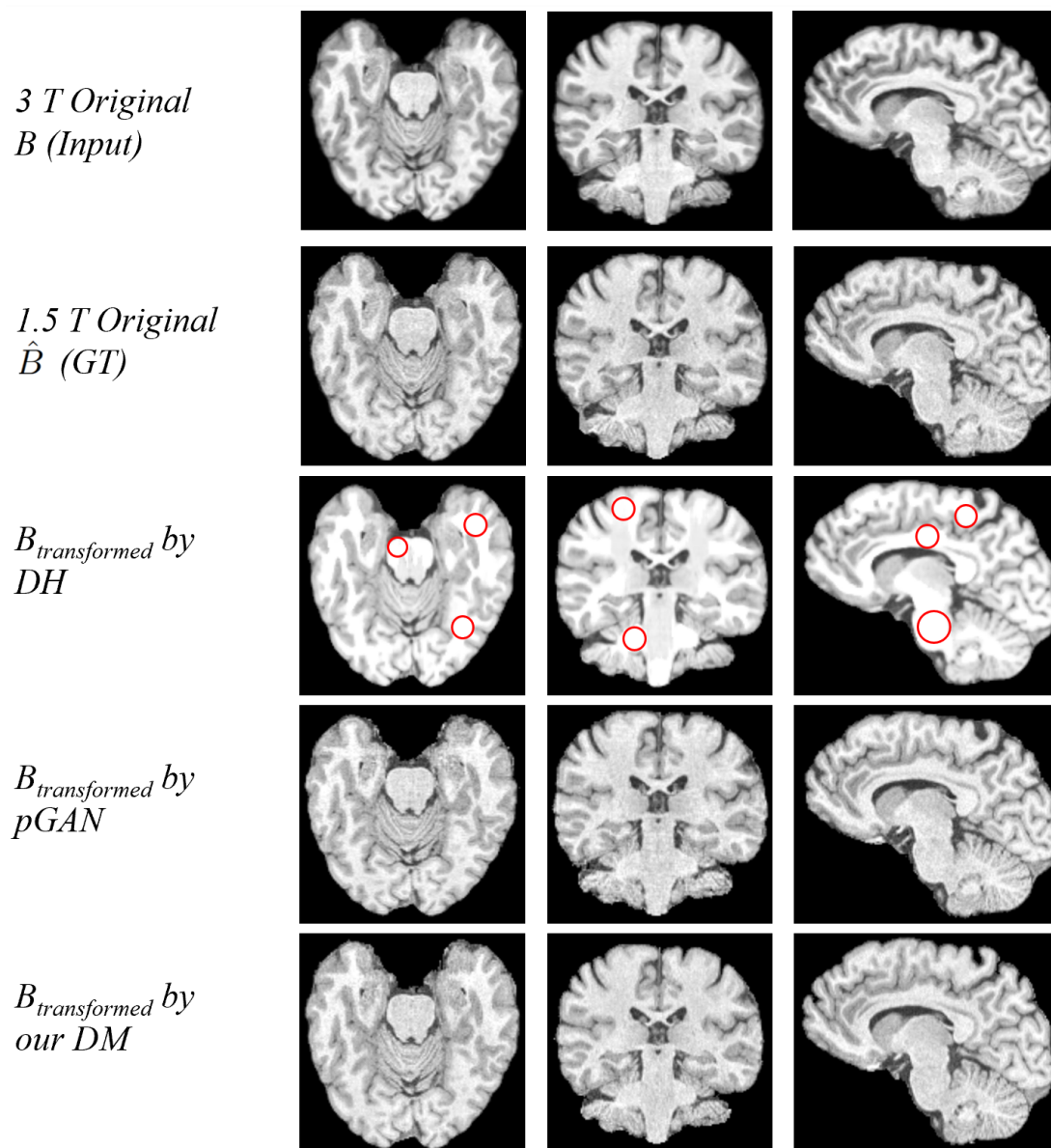


Figure 9: Exemplary images for the translation from 3T source contrast to 1.5T target contrast. The methods generate sagittal slices (right column), which are stacked to create a 3D volume. The red circles indicate hyperintense regions generated by  $DH$ .

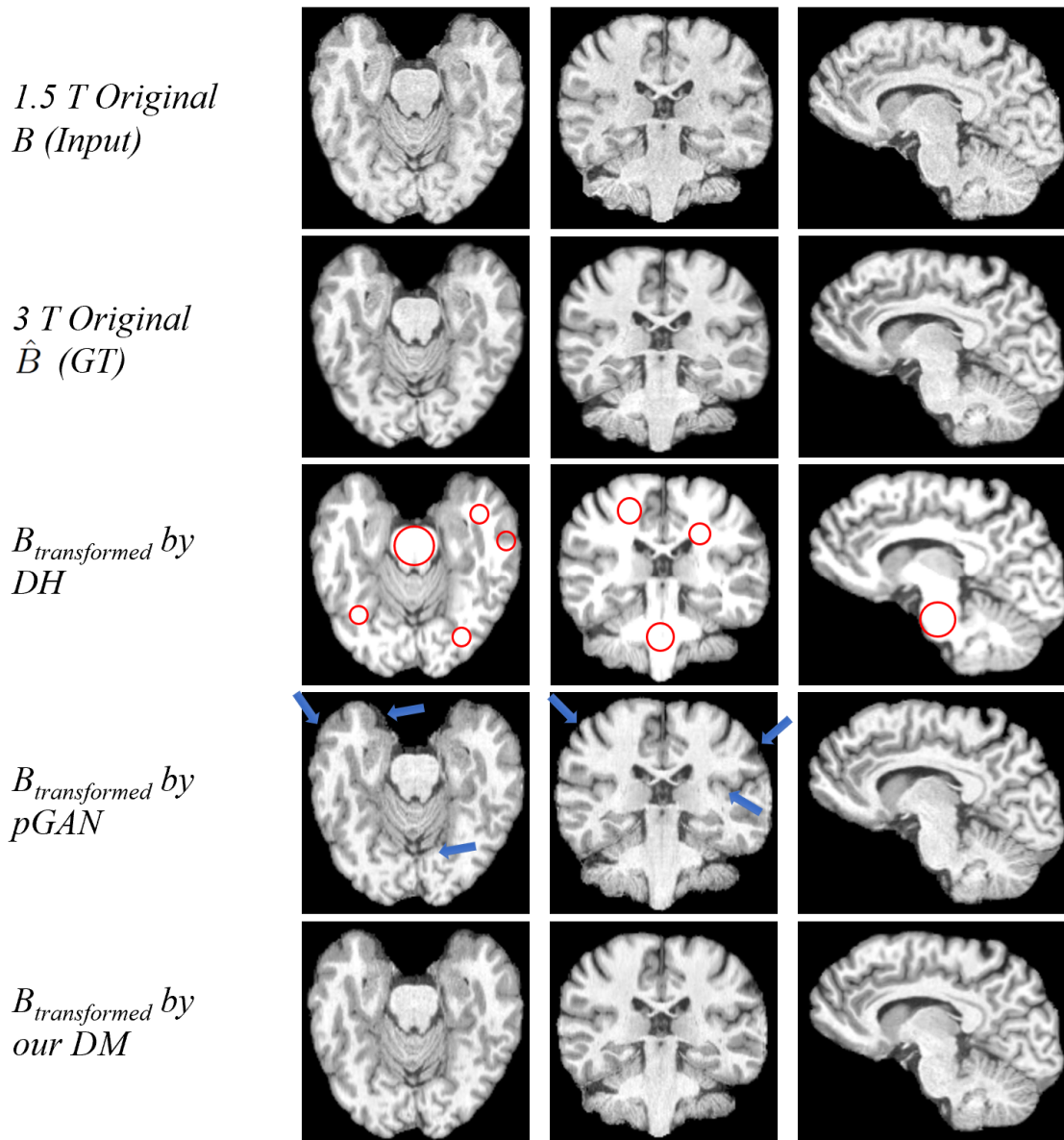


Figure 10: Exemplary images for the translation from 1.5 T source contrast to 3 T target contrast. The methods generate sagittal slices (right column), which are stacked to create a 3D volume. The red circles indicate hyperintense regions generated by  $DH$ . The blue arrows point at stripe artifacts due to the stacking of 2D slices produced by the  $pGAN$ .



## Appendix G. Segmentation Examples

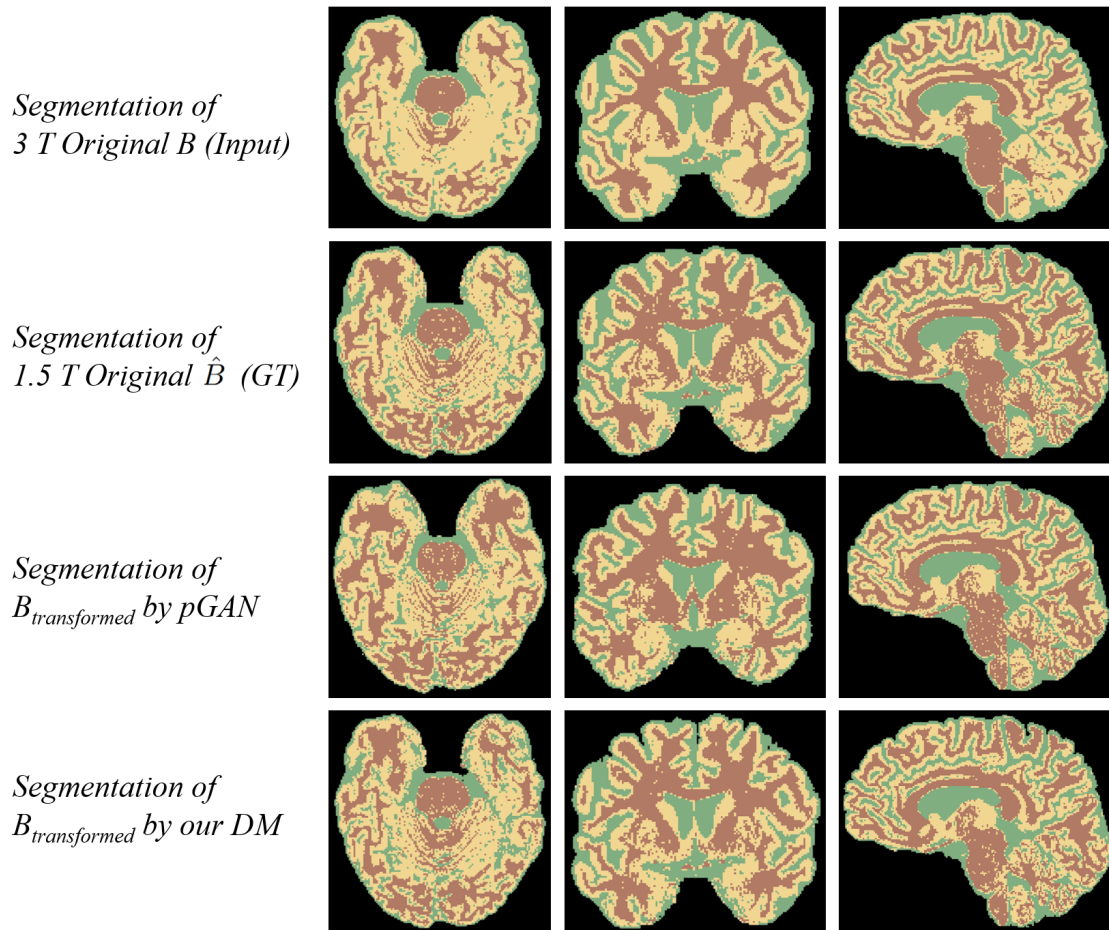


Figure 11: Exemplary segmentations for the translation from 3T source contrast to 1.5T target contrast. Green indicates CSF, yellow is GM and red is WM.

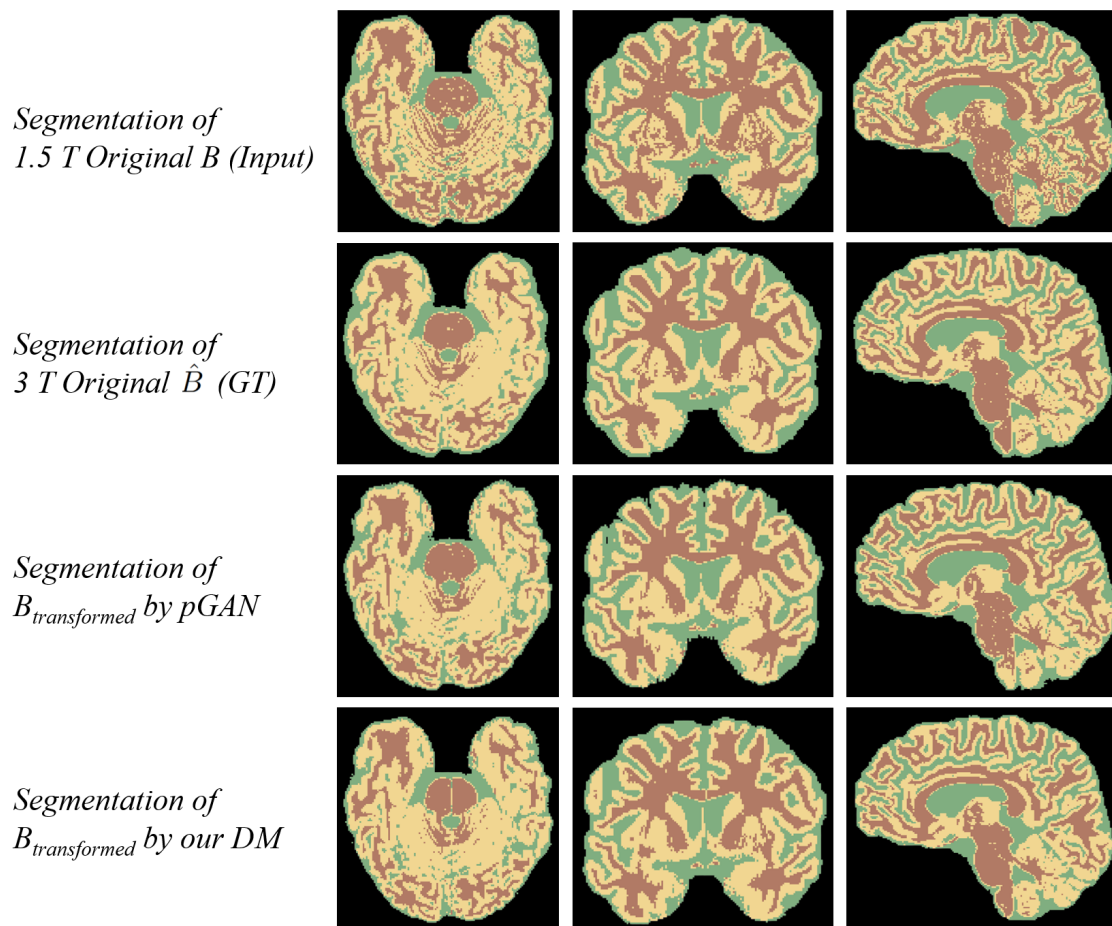


Figure 12: Exemplary segmentations for the translation from 1.5 T source contrast to 3 T target contrast. Green indicates CSF, yellow is GM and red is WM.